ADVANCED ENERGY MATERIALS
www.advenergymat.de

Unraveling Charge Separation and Transport Mechanisms in Aqueous-Processed Polymer/CdTe Nanocrystal Hybrid Solar Cells

Lei Wang, Hai-Yu Wang, Hao-Tong Wei, Hao Zhang, Qi-Dai Chen, Huai-Liang Xu, Wei Han, Bai Yang,* and Hong-Bo Sun**

Recently great progress has been achieved in highly effective hybrid solar cells fabricated using aqueous materials. The state-of-the-art energy conversion efficiency has been close to 5% with high photocurrent. However, charge separation and transport mechanism in the aqueous-processed hybrid solar cells are rarely reported and are usually assumed to be similar to oil-phase processed systems; that is, self-assembly polymers are mainly responsible for charge separation and carrier transport. To date, this assumption has prohibited further improvement of the conversion efficiency in aqueous-processed hybrid systems by adopting any appropriate technique routes. Here, ultrafast carrier dynamics in these hybrid solar cells consisting of poly(*p*-phenylenevinylene) (PPV)-based aqueous polymers and water-solution CdTe nanocrystals (NCs) are investigated in detail. Self-charge separation in grown CdTe NC partly capped CdS shell layers after anneal treatment is unambiguously identified. Different from their oil-soluble counterparts, these core/shell nanocrystals do not have the restrictions of quantum confinement and surface ligands, form effective charge transport networks, and play a dominant role in the charge separation and carrier transport processes. These findings provide a greater understanding on the fundamental photophysics in aqueous-processed hybrid systems.

1. Introduction

Combining organic polymers with inorganic semiconductor nanomaterials to form hybrid solar cells is an attractive concept to achieve the goal of next generation solar cells with low-cost and high power conversion efficiency.[1–3] In these attempts, it is expected that by taking advantage of the unique properties of both materials, the hybrid photovoltaic cells can be endowed with flexibility from polymers and high charge mobility from semiconductor nanocrystals (NCs).[4] One feasible proposal is replacing the typical acceptor materials in organic solar cells, i.e., fullerene derivates, by semiconductor nanocrystals.[5] Since the absorption of fullerene derivates contributes little to the photocurrent in high effective organic photovoltaic devices, this simple replacement was thought to be great benefit for the improvement of device performance. Several approaches were developed to improve the interfacial contact in practical polymer/nanocrystal hybrid solar cells field.[6–12] One main difficulty is gradually realized that the separated charges in semiconductor nanocrystals could not effectively transport to the electrode as expected, despite the charge separation in the interfaces between polymer and nanocrystal is indeed substantial.[13–16] To further boost device performance, development of new low band gap polymers,[17,18] optimization of polymer and nanocrystal morphology,[19–21] and introduction of new carrier transport materials such as carbon nanotubes,[22] have been reported. Nevertheless, due to the

L. Wang, Prof. H.-Y. Wang, Prof. Q.-D. Chen, Prof. H.-L. Xu, Prof. H.-B. Sun
State Key Laboratory on Integrated Optoelectronics
College of Electronic Science and Engineering
Jilin University
2699 Qianjin Street
Changchun 130012, China
E-mail: haiyu_wang@jlu.edu.cn; hbsun@jlu.edu.cn
Prof. W. Han, Prof. H.-B. Sun
College of Physics, Jilin University
2699 Qianjin Street
Changchun 130023, China
H.-T. Wei, Prof. H. Zhang, Prof. B. Yang
State Key Laboratory of Supramolecular Structure and Materials
College of Chemistry
Jilin University
2699 Qianjin Street
Changchun 130023, China
E-mail: byangchem@jlu.edu.cn

DOI: 10.1002/aenm.201301882

complex interfacial environment, high charge mobility of semiconductor nanocrystals was also sacrificed to some extent.[23–26]

The advent of aqueous-processed polymer/nanocrystals hybrid solar cells becomes an alternative approach to achieve high energy conversion efficiency.[27,28] These photovoltaic devices not only consider the green chemistry concept, but also provide different design rules in comparison with their oil-soluble counterparts.[29] Some recent progresses are extremely fascinating. First, due to the unique properties of short-chain ligands on water-solution nanocrystals, aqueous-solution-processed hybrid solar cells have better thermal and morphological stability.[30] Previous work realized that the diameter of water-solution CdTe quantum dots increased from 2.8 nm to tens of nanometers owing to annealing-induced growth.[31] This was ascribed to the removal of surface ligands in the process of annealing. Hence, it was thought to be responsible for better carrier transport between nanocrystals in the vicinity without other chemical treatments. Second, beyond quantum confinement, the band gap of grown nanocrystals is similar to bulk material, which furthest increases the range of absorption spectrum and thus improves the photocurrent of devices.[32,33] Last but not least, the designed device structure strongly affects device performance.[34] Recently, it was reported that inverted aqueous-solution-processed poly(*p*-phenylenevinylene) (PPV)/CdTe NCs hybrid solar cells obtain a power conversion efficiency (PCE) of 3.75% in planar heterojunction, which is comparable with the bulk-heterojunction devices, and a record PCE of 4.76% with maximum photocurrent over 16 mA cm^{-2} in n–i structure.[35] All of these imply the charge separation and carrier transport in aqueous-processed hybrid systems are highly effective, and likely different from oil-phase processed systems.

Here, we make detailed researches on the charge separation and transport mechanism in two kinds of typical aqueous-processed hybrid solar cells consisting of aqueous polymers PPV (or poly[(3,4-dibromo-2,5-thienylenevinylene)-*co*-(p-phenylenevinylene)] (PBTPV)) and water-solution CdTe nanocrystals.[35,36] Their molecule structure and type II energy level arrangement among polymers and CdTe nanocrystals are presented in **Figure 1**. Using a combination of femtosecond time-resolved fluorescence dynamics measured by the fluorescence upconversion technique and femtosecond broadband transient absorption (TA) spectroscopy, the photophysics of aqueous polymer films are investigated. Then, neat water solution CdTe NC films are found to have self-charge separation property due to the formation of CdS shell in the processes of heat-anneal treatment. Finally, charge separation and carrier transport processes in aqueous-processed hybrid photovoltaic systems are unambiguously unraveled, and the crucial factors that could improve the device performance in future are further discussed.

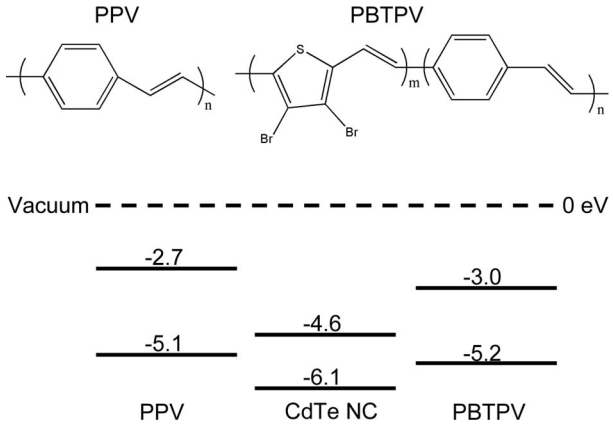

Figure 1. a) Molecular structure and b) type II energy level arrangement for polymers and CdTe nanocrystals.

2. Results and Discussion

2.1. Steady-State Absorption and Photoluminescence

Figure 2a shows the steady-state absorption spectra of annealed polymers, CdTe NCs films, and hybrid films with high dopant fraction of CdTe NCs. Unless indicated otherwise, all samples were annealed and encapsulated in the glove box for further experiments. For the organic polymer donors, the absorption spectra of both PPV and PBTPV films are similar for wavelength above 400 nm, in which the absorption peak locates at about 430 nm with a shoulder at 490 nm. Due to the addition of thienylene units, PBTPV film exhibits a larger absorption tail in the range of 500–600 nm. This leads to a weaker but red-shift photoluminescence (PL), in which the center emission wavelength shifts from 550 nm in PPV to 590 nm in PBTPV (Figure 2b). For the inorganic CdTe nanocrystal acceptor, a broad bulk band gap appears at about 1.5 eV (820 nm, average size about 20 nm) after annealing treatment, compared with as-made nanocrystal film with a larger band gap at 2.2 eV (560 nm, average size 2.3 nm) due to the quantum confinement effect (Figure S1, Supporting Information). The emission of polymers is gradually quenched by increasing the weight fraction of CdTe NCs in hybrid films (Figure S2, Supporting Information). For optimized aqueous-processing of hybrid photovoltaic devices (high nanocrystal fraction of CdTe NCs, 97 wt%), the PL of polymer donors is almost totally quenched. It is noteworthy that the PL of CdTe NCs in the formation of solid film is not observed.

2.2. Exciton Transport in Aqueous Polymer Films

Different from oil-phase polymer films, i.e., poly(3-hexylthiophene) (P3HT), aqueous PPV film exhibits a very weak excitation density dependent behavior in 400 nm excitation (**Figure 3**a). This suggests a very fast exciton–exciton annihilation process, and photogenerated excitons are annihilated within 100 ps. This can not be explained by a 3D exciton diffusion model as described previously.[37,38] It implies limited exciton diffusion length in aqueous PPV film, which is not good for charge transport in hybrid films.

For PBTPV film, the pump-intensity dependent carrier dynamics is recovered to a certain extent (Figure 3b). According to multiexponential analysis in the lowest excitation density (the best-fit parameters in **Table 1**), it gives an average PL lifetime of 29 ps for PBTPV film, as nearly three times longer than that of 11 ps for PPV film (Figure S3, Supporting Information). A 3D-diffusion model also can successfully fit these exciton density dependent decay traces. Based on the estimated exciton

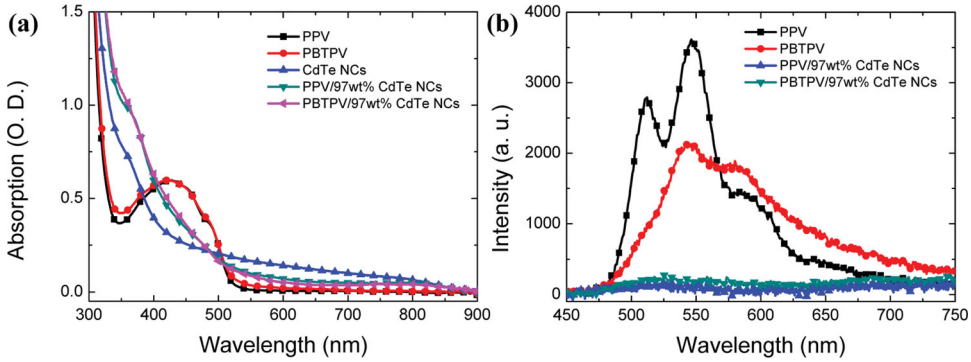

Figure 2. a) Steady-state absorption and b) PL spectra for neat PPV, PBTPV, CdTe NCs, and hybrid films.

density, the global fitting of all five kinetic curves gives two satisfactory fitting parameters together: one is exciton-exciton annihilation radius R_a = 2.2 ± 0.1 nm; the other is isotropic diffusion constant $D = (8.2 \pm 0.6) \times 10^{-3}$ cm^2 s^{-1}. Considering the longest exciton lifetime of 54 ps (τ_3 for PBTPV in Table 1), the diffusion length and annihilation rate constant were then estimated to be $L_D = \sqrt{D\tau_3}$ = 6.6 ± 0.3 nm and $\gamma = 4\pi R_a D = 2.3 \times 10^{-8}$ cm^3 s^{-1}, respectively. The isotropic diffusion constant is one order of magnitude larger than oil-phase polymers, i.e., P3HT.[37] But it also leads to a large exciton annihilation rate, which shortens its exciton lifetime. As a result, exciton diffusion length is still limited.

We also utilized femtosecond transient absorption spectroscopy to investigate the optical properties of these aqueous polymer films (**Figure 4**). In 400 nm excitation, both PPV and PBTPV films clearly show three ground state bleaching peaks (negative signals) at 430 nm, 455 nm and 490 nm, which correspond to 0–0, 0–1 and 0–2 vibration transitions, respectively. In spite of the spectral overlapping between the excited-state absorption (positive signal) and stimulated emission (negative signal) for longer wavelength range, an evolution of stimulated emission signal can be observed in PBTPV films. These indicate that the addition of 3,4-dibromo-2,5-thienylenevinylene units in PBTPV does not break the PPV backbone, but it indeed changes the excited-state properties of films. Interestingly, according to the TA dynamics at 490 nm and 525 nm, PBTPV film has a smaller oscillation amplitude and slightly shorter respond period than PPV film (Figure 4c,d). This breath mode originates from the longitudinal propagating strain waves in the film after photoexcitation.[39,40] Ignoring the difference of film thickness and absorption coefficient at 400 nm between PBTPV and PPV and assuming both polymers have same deformation potential, our TA results imply the average longitudinal strain in the PBTPV film is about four times smaller than that in PPV film.

2.3. Charge Transport in Grown CdTe NC Network

After investigating the photophysics of aqueous donor polymers, we further studied the acceptor CdTe NC films by femtosecond transient absorption in 400 nm and 800 nm excitation (**Figure 5**). Both transient spectra give a large and distinct ground state bleaching signal at 825 nm. This is assigned to the band edge of grown CdTe NCs. As expected, it is consistent with the band gap in steady-state absorption spectra. But another small and clear bleaching signal at 510 nm appears in TA, which is "invisible" in steady-state absorption spectra. As-made CdTe NCs are not responsible for this bleaching signal because their ground state bleaching signal in TA is located at 560 nm (Figure S4, Supporting Information). In addition, the annealing-induced growth also could not generate smaller nanoparticles.[31] Hence, this bleaching signal is not from CdTe NC itself. Instead, we find that it is in agreement with the band gap of bulk CdS.[41,42] It can be understood that the annealing process facilitates the growth of CdTe NCs and removes both the interfacial and excess ligands on CdTe NCs, and also induces

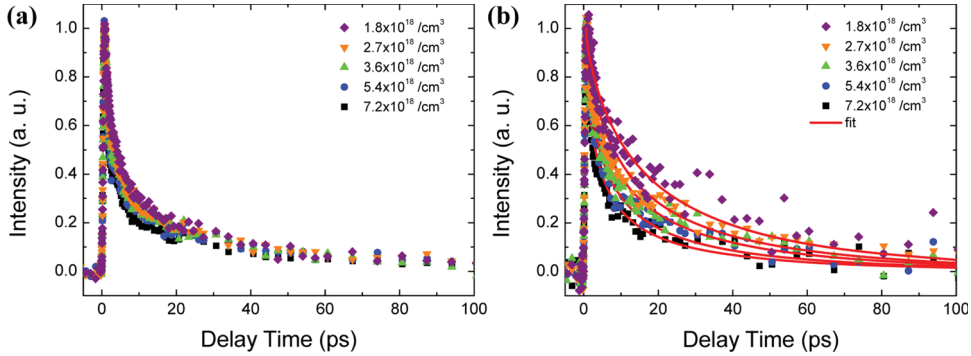

Figure 3. Pump intensity dependent femtosecond time-resolved PL dynamics for a) neat PPV film probed at 550 nm and b) PBTPV film probed at 590 nm in 400 nm excitation. Red solid lines represent the fitting results by 3D diffusion model.

Table 1. Femtosecond time-resolved PL dynamics by multi-exponential fitting.

Materials	τ_1 [ps]	τ_2 [ps]	τ_3 [ps]	τ_{ave} [ps]	$\eta_{PL\ quenching}$
PPV	0.6 (0.40)	4.4 (0.37)	40 (0.23)	11	
PPV/30 wt% CdTe NCs	0.2 (0.58)	3.2 (0.29)	23 (0.13)	4.0	0.64
PPV/60 wt% CdTe NCs	0.8 (0.65)	7.0 (0.35)		3.0	0.73
PPV/97 wt% CdTe NCs	0.7 (0.66)	3.6 (0.34)		1.7	0.84
PBTPV		3.7 (0.50)	54 (0.50)	29	
PBTPV/97 wt% CdTe NCs		2.9 (0.81)	39 (0.19)	9.8	0.66

the growth of CdS shell on the surface of grown CdTe NCs. Additionally, the small amplitude of CdS state implies its partly capped shell structure.

A type-II CdTe/CdS band structure in bulk materials and core/shell quantum dots has been demonstrated by previous theoretical and experimental work.[42,43] Therefore, for these grown nanocrystals, the type-II band structure is also expected. In 400 nm excitation experiment, after hot carriers cooling, photoinduced electrons and holes fill in both CdTe core and CdS shell. So the two ground-state bleaching signals are assigned to $CdTe_{1S}$ state and CdS_{1S} state, respectively (Figure 5a). Both states decay much quickly with half-lifetime of 7–8 ps (Figure 5c). Meanwhile, the arising time (state-filling time) of $CdTe_{1S}$ state (≈3 ps) is twice as long as that of CdS_{1S} state. According to our previous study, this change could be attributed to hole transfer from CdS shell to CdTe core.[43] On the other hand, in 800 nm excitation experiment, the band edge of grown CdTe NCs is directly pumped. Photoinduced holes are confined in CdTe, and photoinduced electrons can easily tunnel into CdS in the vicinity. Thus, the type-II band structure in grown CdTe/CdS NCs lacking of quantum confinement is clearly demonstrated, and the two ground-state bleaching signals are assigned to $CdTe_{1S}$ state and CdS^- state, respectively (Figure 5b). In this case, the decay traces of the two states are almost the same with a longer half-lifetime of 80–100 ps (Figure 5d). This different decay dynamics corresponding to CdTe and CdS states between 400 nm and 800 nm excitation experiments implies that in the process of cooling, hot carriers, especially for hot holes, maybe undergo many trap levels, which could be located between the valence band minimum of CdTe and CdS.[43] This unambiguously indicates the self-assemble CdTe/CdS NCs networks prefer to transport electrons rather than holes. Additionally, these traps may be the main reason for the PL quenching of CdTe NCs solid films. Our work provides a thorough investigation of the electronic character of grown nanocrystal solids, and hence it is of great significance to further achieving improvements in performance through elimination of these detrimental hole trap states.

2.4. Charge Separation and Transport in Aqueous-Processed Hybrid Photovoltaic Systems

To scrutinize the charge separation in hybrid films, we utilized femtosecond time-resolved fluorescence dynamics in 400 nm

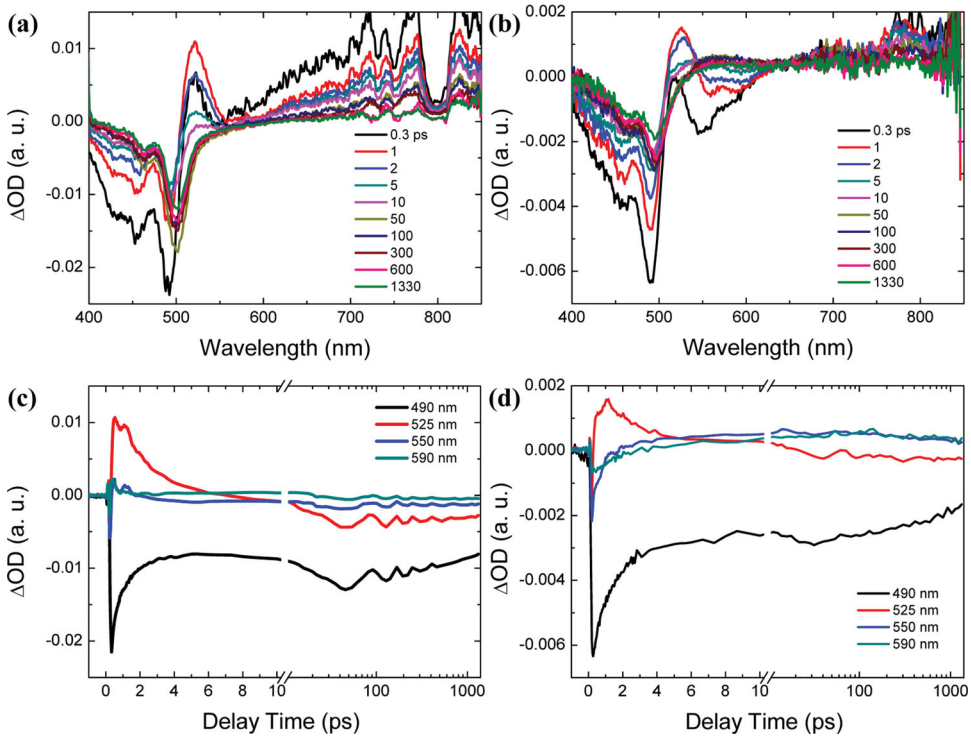

Figure 4. Transient absorption spectra and characteristic dynamics for a,c) neat PPV film and b,d) PBTPV film in 400 nm excitation.

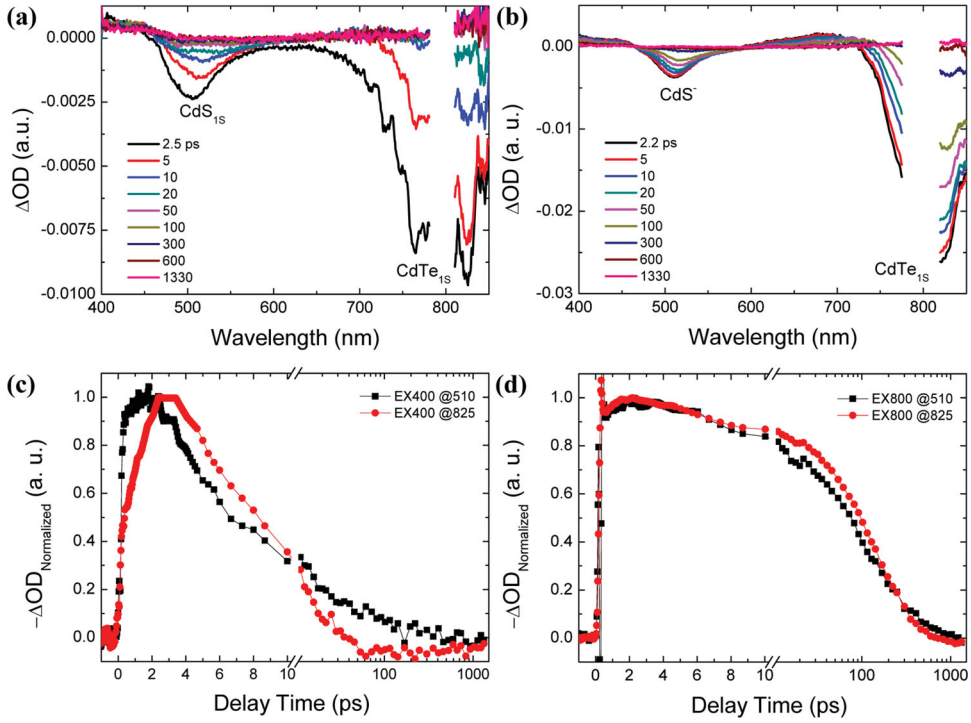

Figure 5. Transient absorption spectra and characteristic dynamics for neat CdTe film in a,c) 400 nm and b,d) 800 nm excitation.

excitation to explore the PL quenching dynamics of donor polymers, which indicates the electron transfer or energy transfer from polymers to CdTe NCs (**Figure 6**).

PL quenching dynamics of donor polymer is acceptor-concentration dependent taken PPV/CdTe NCs hybrid films for example as shown in Figure 6a. The best multiexponential fitting parameters are list in Table 1. The average PL lifetimes are 4 ps, 3 ps and 1.7 ps for nanocrystal fraction of 30 wt%, 60 wt% and 97 wt%, respectively. The corresponding PL quenching efficiency ($\eta_{\text{PL quenching}} = 1 - \tau_{\text{PPV-NC}}/\tau_{\text{PPV}}$) is estimated as high as 64%, 73% and 84%, respectively. This is consistent with the steady-state PL quenching experiments (Figure S2, Supporting Information). For the same highest nanocrystal fraction, PBTPV/CdTe NCs film shows slower PL quenching rate (1/9.8 ps^{-1}) and lower PL quenching efficiency (66%) than PPV/CdTe NCs film (Figure 6b). This is contributed to reduced driving force for electron transfer and lower PL quantum yield for energy transfer.

As a necessary complement, femtosecond broadband transient absorption experiments at 800 nm excitation are performed to observe the possible hole transfer from CdTe NCs to polymers (**Figure 7**). Transient spectral features for both hybrid films are similar to neat CdTe NCs, but the decay dynamics are faster due to the expected hole transfer (Figure 7c). Half-lifetime for $CdTe_{1S}$ state in PPV/CdTe NCs and PBTPV/CdTe NCs is decreasing to 6 ps and 16 ps, respectively, compared to the half-lifetime of 100 ps in neat CdTe NCs. This slower hole separation rate in PBTPV/CdTe NCs also results from reduced driving force for hole transfer.

Both PL quenching experiments and selective excitation experiments of CdTe NCs demonstrate the contribution of driving force to charge separation is much larger than the

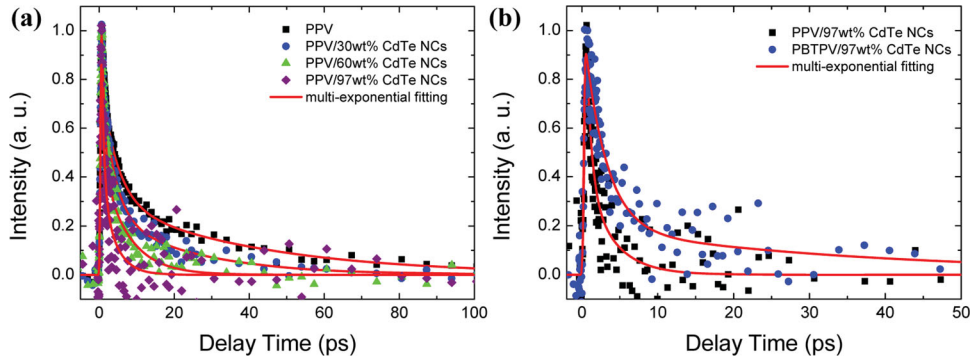

Figure 6. Femtosecond time-resolved PL dynamics for a) PPV/CdTe NC film with different nanocrystal concentration probed at 550 nm and b) PBTPV/97 wt% CdTe NC film probed at 590 nm in 400 nm excitation (pump density: 1.8×10^{18} cm^{-3}). Red solid lines represent the multi-exponential fitting results.

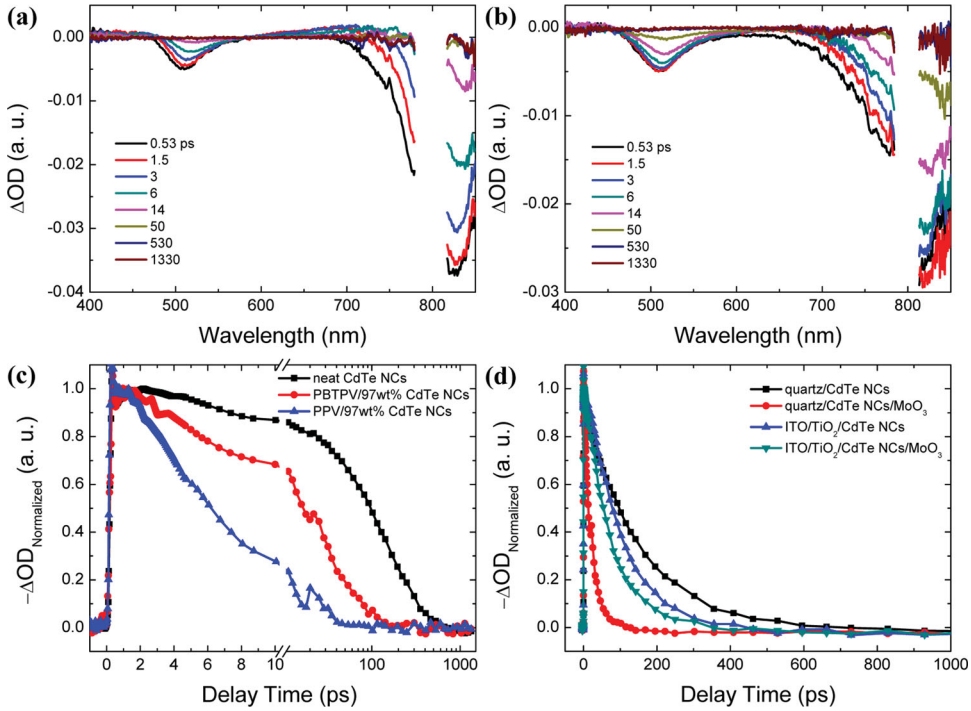

Figure 7. Transient absorption spectra for a) PPV/97 wt% CdTe film and b) PBTPV/97 wt% CdTe film in 800 nm excitation. c) Characteristic dynamics of $CdTe_{1S}$ state in neat CdTe NCs, PBTPV/97 wt% CdTe and PPV/97 wt% CdTe film. d) Characteristic dynamics of $CdTe_{1S}$ state in neat CdTe NCs, CdTe NCs with evaporation of MoO_3, CdTe NCs spin-coated on TiO_2 modified ITO electrode, and CdTe NCs with both electron (TiO_2) and hole (MoO_3) transport layers. All these characteristic dynamics of $CdTe_{1S}$ state are probed at 825 nm with 800 nm excitation.

interaction between polymer and nanocrystal. Although S atoms on the thiophene rings of PBTPV are expected to provide more effective coordination to the CdTe NCs,[36] the only 0.1 eV difference of driving force for hole transfer still determines the faster hole transfer rate in PPV/CdTe NCs. This could arise from partly capped CdS shell, which passivates most surface Cd atoms.

Since grown CdTe NCs partly capped CdS not only possess of excellent ability of self-charge separation, but also construct effective free carrier transport networks, we further conduct a series of experiments on neat CdTe NCs with modified electrodes to study the charge transport processes between CdTe NCs active layer and electrodes (details of sample fabrication seen in Experimental Section). TiO_2 and MoO_3 are adopted as typical electron transport layer and hole transport layer on the surface of electrodes. These feature dynamics of $CdTe_{1S}$ state in 800 nm excitation are presented in Figure 7d. Using quartz/CdTe NCs with half-lifetime of 100 ps as blank experiment, CdTe NCs spin-coated on TiO_2 modified ITO electrode (ITO/TiO_2/CdTe NCs) show slightly faster decay with half-lifetime of 75 ps. It implies electron transfers from CdTe NCs networks to the electrode interface. Since the conduction band bottom of TiO_2 is slightly higher than that of CdTe NCs, most free electrons close to the conduction band bottom of CdTe NCs are firstly transfer into defect states in the band gap of TiO_2, then transport to the ITO electrode. This barely satisfactory electron transport suggests great potential for improvement of electron transport by more suitable surface modification on ITO electrode, for example, adopting UV-irradiated TiO_2 nanorod as buffer layer,[44,45] or replacing TiO_2 by graphene or reduced graphene oxide.[46,47] On the other hand, CdTe NCs with evaporation of MoO_3 (quartz/CdTe NCs/MoO_3) presents very faster decay with half-lifetime of 14 ps. This highly effective hole transport explains the improvement of device performance in typical inverted structure.[34,36] Noted that we have indicated the possibility of the existence of hole traps at the interface between the CdTe NCs and CdS shell, eliminating these surface states as much as possible will be helpful for enhancement of hole mobility. Moreover, development of new low band gap aqueous polymers with better hole capture ability is another solution because the main duty of aqueous polymers is hole transferring and transport. However, as we discovered above, the exciton diffusion length in polymer networks is still short (i.e., 6.6 nm for PBTPV). Thus, it results in only part of polymers close to the hole transport layer that can transport holes to electrode, despite that hole separation occurred in any possible location. This explains why the performance in planar heterojunction device is similar to that in bulk-heterojunction device.[35] Hence, better hole transport properties for new aqueous polymers or designing new electrode structure for matching these transport properties of aqueous polymers are also very important for improving the photovoltaic device performance. Lastly, for CdTe NCs with both electron and hole transport layers (ITO/TiO_2/CdTe NCs/MoO_3), the decay with half-lifetime of 50 ps is faster than that in only electron transport layer (ITO/TiO_2/CdTe NCs), but it is much slower than that in only hole transport layer (quartz/CdTe NCs/MoO_3). This clearly indicates the built-in electric field resulting from the charge aggregation on the electrodes strongly affects the charge transport in CdTe NCs active layer. Even in current best device structure (inverted structure),

the electron transport layer is still improper. This provides a new technical route for improvement of device performance, in addition to developing new aqueous polymers with larger light-harvesting range as it was done in organic solar cells.

Taken together, our results indicate that grown nanocrystals are the pivotal factor in aqueous-processed hybrid solar cells, since charge generation occurs mainly in the nanocrystals, rather than at the polymer/inorganic interface, which contradicts traditional thoughts in this field. Since the average size of grown CdTe NCs is about 20 nm, while the thickness of hybrid film is about 60–80 nm, it means that there is only 3–4 layers of stacked CdTe NCs in the active layer. With the help of this spontaneous inorganic shell during the annealing process, it indeed facilitates the connection among nanocrystals in vicinity. But it is only beneficial for electron transfer across the whole active layer, since the defect levels located between the valence band minimum of CdTe and CdS become hole traps. This annealing-induced passivation is a common process in aqueous-processed polymer/nanocrystal hybrid solar cells. Other passivated shell is also observed in PPV/$Cd_{0.75}Hg_{0.25}Te$ NCs hybrid film (Figure S5, Supporting Information). At 800 nm excitation, a broad and clear bleaching signal at around 540 nm (2.30 eV) appears in TA, which is also "invisible" in steady-state absorption spectra. Since this bleaching signal locates within range between the bulk band gap of CdS (2.42 eV) and red HgS (2.03 eV), we assign this state to the contribution of $Cd_xHg_{1-x}S$ composite shells.

3. Conclusion

In summary, charge separation and transport mechanism in aqueous-processed polymer/CdTe NCs hybrid solar cells have been studied in detail by ultrafast spectroscopy. It demonstrates that different from oil-soluble polymers, aqueous polymers have large exciton diffusion constant and short exciton lifetime. Self-charge separation in grown CdTe NCs partly capped CdS shell makes the nanocrystal networks have good electron mobility, while most holes are trapped during the cooling process. For hybrid systems, charge separation between polymer and nanocrystals is mainly determined by the driving force. Considering the large extinction coefficient, wide absorption range, high dopant concentration and self-charge separation feature, self-assemble CdTe NCs networks partly capped CdS shell dominate the charge separation and carrier transport processes in aqueous-processed hybrid systems. Since hybrid passivated photovoltaic devices on the basis of colloid PbS quantum dot solid have achieved a certified power conversion efficiency of 7%, we believe the device performance of aqueous-processed hybrid solar cells based on grown core/shell nanocrystal solids also will be gradually improved and likely comparable with best organic solar cells in the future, if these crucial limitations can be solved one by one.[48] Hence, better surface chemical modification on CdTe nanocrystals to reduce surface hole traps, development of new aqueous polymers with better hole capture and transport ability, increasing the thickness of active layer, choosing more suitable electron transport layer and electrode structure are critical factors to further improve device performance of aqueous-processed hybrid solar cells.

4. Experimental Section

Sample Preparation: Water-soluble polymers, PPV and PBTPV, were synthesized and characterized in previous reports.[35,36] The photoactive layer was formed by spin-coating with an aqueous solution including PPV or PBTPV precursor and 2-mercaptoethylamine (MA)-stabilized CdTe NCs with a weight ratio of 1:28 on cleaned ITO-coated glass substrates, and then was annealed at 250 °C for 60 min in a glove box. Typically, a single pure polymer layer with a thickness of about 60 nm was obtained, and a blending layer with a thickness of 80 nm in ambient conditions. For inverted device structure, cleaned ITO-coated glasses were spin-coated with TiO_2 precursor (about 10 nm) and heated at 350 °C for 15 min, which convert the TiO_2 precursor into anatase-phase TiO_2. After spin-coated active layer, the blend film was annealed at 250 °C for 60 min in the glove box, followed by evaporation of MoO_3 (5 nm). All samples were encapsulated in the glove box for further experiments.

Time-Resolved Fluorescence Experiments: Sub-picosecond time-resolved emissions were measured using the femtosecond fluorescence upconversion method. A mode-locked Ti:sapphire laser/amplifier system (Solstice, Spectra-Physics) was used. The output of the amplifier of 1.5-mJ pulse energy, 100 fs pulse width, at 800 nm wavelength is split into two parts; the stronger beam was used to generate excitation light (400 nm pump pulses directly doubled from 800 nm laser pulses). The resulting fluorescence was collected and focused onto a 1 mm thick beta-BaB_2O_4 (BBO) crystal with a cutting angle of 35°. The other part of the amplifier output was sent into an optical delay line and served as the optical gate for the upconversion of the fluorescence. The generated sum frequency light was then collimated and focused into the entrance slit of a 300 mm monochromator. A UV-sensitive photomultiplier tube 1P28 (Hamamatsu) was used to detect the signal. The full width at half maximum of the instrument response function was about 400 fs.

Femtosecond Transient Absorption Setup: In the transient absorption setup, a mode-locked Ti:sapphire laser/amplifier system (Solstice, Spectra-Physics) was used. The output of the amplifier of 1.5-mJ pulse energy, 100 fs pulse width, 250 Hz repetition rate, at 800 nm wavelength is split into two parts; the stronger beam was used to generate desired excitation light. In traditional 400 nm excitation experiments, 400 nm pump pulses directly doubled from 800 nm laser pulses. The broadband white-light probe pulses from 400 nm to 850 nm generated from 2-mm-thick water. The transient absorption data were collected by a fiber-coupled spectrometer connected to a computer. The group velocity dispersion of the transient spectra was compensated by a chirp program. In all TA experiments, the pump intensity was fixed at 50 nJ/pulse for 400 nm and 100 nJ/pulse for 800 nm. All the measurements were preformed at room temperature.

Supporting Information

Supporting Information is available from the Wiley Online Library or from the author.

Acknowledgements

The authors would like to acknowledge National Basic Research Program of China (973 Program, Grant Nos. 2014CB921302 and 2011CB013004), Natural Science Foundation, China (NSFC) under Grant Nos. 21273096, 61376123, and 21221063 for support.

Received: December 7, 2013
Revised: February 6, 2014
Published online:

[1] W. U. Huynh, J. J. Dittmer, A. P. Alivisatos, *Science* **2002**, *295*, 2425.
[2] Y. F. Zhou, M. Eck, M. Krüger, *Energy Environ. Sci.* **2010**, *3*, 1851.
[3] W. U. Huynh, X. G. Peng, A. P. Alivisatos, *Adv. Mater.* **1999**, *11*, 923.
[4] S. Gunes, N. S. Sariciftci, *Inorg. Chim. Acta* **2008**, *361*, 581.

[5] B. Holger, *Energy Environ. Sci.* **2010**, *3*, 1682.
[6] F. Gao, S. Q. Ren, J. P. Wang, *Energy Environ. Sci.* **2013**, *6*, 2020.
[7] M. He, F. Qiu, Z. Q. Lin, *J. Phys. Chem. Lett.* **2013**, *4*, 1788.
[8] H. C. Leventis, S. P. King, A. Sudlow, M. S. Hill, K. C. Molloy, S. A. Haque, *Nano Lett.* **2010**, *10*, 1253.
[9] W. F. Fu, Y. Shi, W. M. Qiu, L. Wang, Y. X. Nan, M. M. Shi, H. Y. Li, H. Z. Chen, *Phys. Chem. Chem. Phys.* **2012**, *14*, 12094.
[10] Y. F. Zhou, F. S. Riehle, Y. Yuan, H. F. Schleiermacher, M. Niggemann, G. A. Urban, M. Krüger, *Appl. Phys. Lett.* **2010**, *96*, 013304.
[11] R. J. Zhou, R. Stalder, D. P. Xie, W. R. Cao, Y. Zheng, Y. X. Yang, M. Plaisant, P. H. Holloway, K. S. Schanze, J. R. Reynolds, J. G. Xue, *ACS Nano* **2013**, *7*, 4846.
[12] H. C. Chen, C. W. Lai, I. C. Wu, H. R. Pan, I. W. P. Chen, Y. K. Peng, C. L. Liu, C. H. Chen, P. T. Chou, *Adv. Mater.* **2011**, *23*, 5451.
[13] N. C. Greenham, X. G. Peng, A. P. Alivisatos, *Phys. Rev. B* **1996**, *54*, 17628.
[14] A. A. Lutich, G. X. Jiang, A. S. Susha, A. L. Rogach, F. D. Stefani, J. Feldmann, *Nano Lett.* **2009**, *9*, 2636.
[15] J. Albero, E. Martínez-Ferrero, J. Ajuria, C. Waldauf, R. Pacios, E. Palomares, *Phys. Chem. Chem. Phys.* **2009**, *11*, 9644.
[16] M. D. Heinemann, K. von Maydell, F. Zutz, J. Kolny-Olesiak, H. Borchert, I. Riedel, J. Parisi, *Adv. Funct. Mater.* **2009**, *19*, 3788.
[17] S. Dayal, N. Kopidakis, D. C. Olson, D. S. Ginley, G. Rumbles, *Nano Lett.* **2010**, *10*, 239.
[18] Y. F. Zhou, M. Eck, C. Veit, B. Zimmermann, F. Rauscher, P. Niyamakom, S. Yilmaz, I. Dumsch, S. Allard, U. Scherf, M. Krüger, *Sol. Energy Mater. Sol. Cells* **2011**, *95*, 1232.
[19] S. Q. Ren, L. Y. Chang, S. K. Lim, J. Zhao, M. Smith, N. Zhao, V. Bulovi , M. Bawendi, S. Gradecak, *Nano Lett.* **2011**, *11*, 3998.
[20] K. F. Jeltsch, M. Schädel, J. B. Bonekamp, P. Niyamakom, F. Rauscher, H. W. A. Lademann, I. Dumsch, S. Allard, U. Scherf, K. Meerholz, *Adv. Funct. Mater.* **2012**, *22*, 397.
[21] Y. Wu, G. Q. Zhang, *Nano Lett.* **2010**, *10*, 1628.
[22] J. M. Lee, B. H. Kwon, H. I. Park, H. Kim, M. G. Kim, J. S. Park, E. S. Kim, S. Yoo, D. Y. Jeon, S. O. Kim, *Adv. Mater.* **2013**, *25*, 2011.
[23] J. E. Brandenburg, X. Jin, M. Kruszynska, J. Ohland, J. Kolny-Olesiak, I. Riedel, H. Borchert, J. Parisi, *J. Appl. Phys.* **2011**, *110*, 064509.
[24] A. Moulé, L. L. Chang, C. Thambidurai, R. Vidu, P. Stroeve, *J. Mater. Chem.* **2012**, *22*, 2351.
[25] K. M. Noone, S. Subramaniyan, Q. F. Zhang, G. Z. Cao, S. A. Jenekhe, D. S. Ginger, *J. Phys. Chem. C* **2011**, *115*, 24403.
[26] N. Radychev, I. Lokteva, F. Witt, J. Kolny-Olesiak, H. Borchert, J. Parisi, *J. Phys. Chem. C* **2011**, *115*, 14111.
[27] Q. Q. Qiao, J. T. McLeskey, *Appl. Phys. Lett.* **2005**, *86*, 153501.
[28] Z. X. Fan, H. Zhang, W. L. Yu, Z. Y. Xing, H. T. Wei, Q. F. Dong, W. J. Tian, B. Yang, *ACS Appl. Mater. Interfaces* **2011**, *3*, 2919.
[29] H. T. Wei, H. Zhang, H. Z. Sun, B. Yang, *Nano Today* **2012**, *7*, 316.
[30] Z. L. Chen, H. Zhang, Z. Y. Xing, J. D. Hou, J. Li, H. T. Wei, W. J. Tian, B. Yang, *Sol. Energy Mater. Sol. Cells* **2013**, *109*, 254.
[31] W. L. Yu, H. Zhang, H. R. Tian, H. T. Wei, W. X. Liu, J. Zhu, J. H. Zhang, B. Yang, *J. Phys. Chem. C* **2012**, *116*, 1322.
[32] H. T. Wei, H. Zhang, H. Z. Sun, W. L. Yu, Z. L. Chen, L. Y. Cui, W. J. Tian, B. Yang, *J. Mater. Chem.* **2012**, *22*, 17827.
[33] W. L. Yu, H. Zhang, Z. X. Fan, J. H. Zhang, H. T. Wei, D. Zhou, B. Xu, F. H. Li, W. J. Tian, B. Yang, *Energy Environ. Sci.* **2011**, *4*, 2831.
[34] Z. L. Chen, H. Zhang, W. L. Yu, Z. B. Li, J. D. Hou, H. T. Wei, B. Yang, *Adv. Energy Mater.* **2013**, *3*, 433.
[35] Z. L. Chen, H. Zhang, X. H. Du, X. Cheng, X. G. Chen, Y. Y. Jiang, B. Yang, *Energy Environ. Sci.* **2013**, *6*, 1597.
[36] H. T. Wei, H. Zhang, G. Jin, T. Y. Na, G. Y. Zhang, X. Zhang, Y. Wang, H. Z. Sun, W. J. Tian, B. Yang, *Adv. Funct. Mater.* **2013**, *23*, 4035.
[37] H. Wang, H. Y. Wang, B. R. Gao, L. Wang, Z. Y. Yang, X. B. Du, Q. D. Chen, J. F. Song, H. B. Sun, *Nanoscale* **2011**, *3*, 2280.
[38] L. Wang, C. F. Wu, H. Y. Wang, Y. F. Wang, Q. D. Chen, W. Han, W. P. Qin, J. McNeill, H. B. Sun, *Nanoscale* **2013**, *5*, 7265.
[39] C. Thomsen, J. Strait, Z. Vardeny, H. J. Maris, J. Tauc, J. J. Hauser, *Phys. Rev. Lett.* **1984**, *53*, 989.
[40] G. S. Kanner, Z. V. Vardeny, B. C. Hess, *Phys. Rev. B* **1990**, *42*, 5403.
[41] D. W. Niles, H. Höchst, *Phys. Rev. B* **1990**, *41*, 12710.
[42] S. H. Wei, S. B. Zhang, A. Zunger, *J. Appl. Phys.* **2000**, *87*, 1304.
[43] L. Wang, H. Y. Wang, B. R. Gao, L. Y. Pan, Y. Jiang, Q. D. Chen, W. Han, H. B. Sun, *IEEE J. Quantum Electron.* **2011**, *47*, 1177.
[44] A. Loiudice, A. Rizzo, L. De Marco, M. R. Belviso, G. Caputo, P. D. Cozzoli, G. Gigli, *Phys. Chem. Chem. Phys.* **2012**, *14*, 3987.
[45] C. Giansante, L. Carbone, C. Giannini, D. Altamura, Z. Ameer, G. Maruccio, A. Loiudice, M. R. Belviso, P. D. Cozzoli, A. Rizzo, G. Gigli, *J. Phys. Chem. C* **2013**, *117*, 13305.
[46] X. Chen, B. H. Jia, Y. N. Zhang, M. Gu, *Light: Sci. Appl.* **2013**, *2*, e92.
[47] J. M. Yun, J. S. Yeo, J. Kim, H. G. Jeong, D. Y. Kim, Y. J. Noh, S. S. Kim, B. C. Ku, S. I. Na, *Adv. Mater.* **2011**, *23*, 4923.
[48] A. H. Ip, S. M. Thon, S. Hoogland, O. Voznyy, D. Zhitomirsky, R. Debnath, L. Levina, L. R. Rollny, G. H. Carey, A. Fischer, K. W. Kemp, I. J. Kramer, Z. J. Ning, A. J. Labelle, K. W. Chou, A. Amassian, E. H. Sargent, *Nat. Nanotechnol.* **2012**, *7*, 577.